ORNL/TM-166393

Ytterbium Ion Collection on Graphite Plates

Brent Dial
Jenny Conner
Harry Meyer III
Shannon Mahurin
Brenda Smith

May 2022

OAK RIDGE National Laboratory

ORNL IS MANAGED BY UT-BATTELLE LLC FOR THE US DEPARTMENT OF ENERGY

ORNL/TM-166393

Enrichment Science and Engineering Division

YTTERBIUM ION COLLECTION ON GRAPHITE PLATES

Brent Dial
Jenny Conner
Harry Meyer III
Shannon Mahurin
Brenda Smith

May 2022

Prepared by
OAK RIDGE NATIONAL LABORATORY
Oak Ridge, TN 37831-6283
managed by
UT-BATTELLE LLC
for the
US DEPARTMENT OF ENERGY
under contract DE-AC05-00OR22725

CONTENTS

LIST OF FIGURES

LIST OF TABLES

ABBREVIATIONS

C	carbon
EDS	energy dispersive x-ray spectroscopy
EMIS	electromagnetic isotope separation
F	fluorine
FWHM	full width half maximum
Na	sodium
O	oxygen
SEM	scanning electron microscopy
Si	silicon
XPS	x-ray photoelectron spectroscopy
Yb	ytterbium

ABSTRACT

Surface characterization and analysis of the graphite collection and strike plates was conducted in this report. These plates were from an electromagnetic isotope separation collector that had been irradiated with an ytterbium ion beam. The results of this study are reported along with analysis and discussion of the potential growth mechanism of the ytterbium layer on graphite. It is proposed that directional deposition of ytterbium ions occurs first in the defect regions of the graphite plate. As deposition continues, it leads to the eventual formation of directional globs that elongate and grow into (1) plates, (2) then stacks, and (3) finally into sheets of ytterbium. The ytterbium layer appears to have a definite phase boundary with the graphite layer. It was also determined that during irradiation with the ytterbium ion beam, the sputtered carbon becomes interpolated in the ytterbium surface layer on the graphite plate and has an amorphous microstructure.

1. INTRODUCTION

This report aligns with the ongoing efforts of the Stable Isotope Material and Chemistry Group to support, improve, and advance the technology used for enrichment of stable isotopes through electromagnetic isotope separation (EMIS).[1-4] The EMIS is used to separate and enrich isotopes. As the ion beam travels through the device, the isotopes are separated and then collected. This report focuses on the supporting material for the collection stage of the enrichment process.[5, 6] During the collection stage, enriched isotopes traveling in 40 keV ion beam are collected in pockets made of graphite plates. The beam travels into the pockets and impacts a strike plate. This cause the ions and atoms on the strike plate to be sputtered and collected on adjacent plates within the pocket (i.e., collection plates). In this study, the properties of the collection and strike plates were characterized before and after irradiation with an Yb ion beam. The surfaces of a pristine graphite plate, as well as irradiated collection and strike plates were characterized for comparison using SEM, EDS, XPS, and Raman. The pristine and irradiated collection and strike plates were broken into smaller sections (Figure 2) to fit into the analytical tools' sample chambers. As demonstrated, the Yb ion beam enters the collector at column A and strikes a graphite bar (i.e., the strike plate) at the edge of column D, where sputtering occurs and generates a plume of secondary particles that deposit across the collection plates. The highest intensity of sputter particles are observed in column D and rows 2 and 3 of the collection plate (see Figure 2, left).

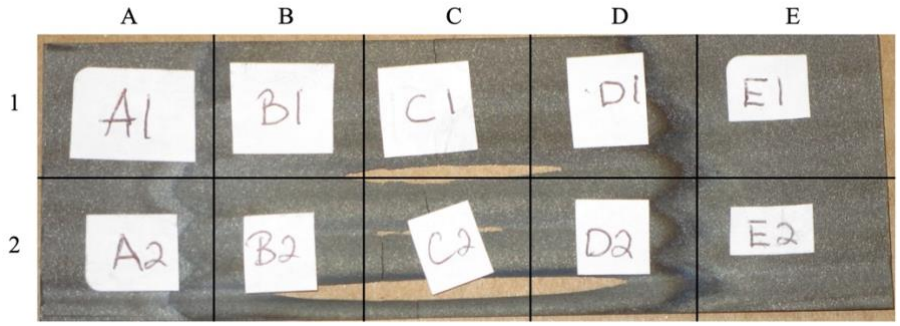

Figure 1. Strike plate after ion beam irradiation.

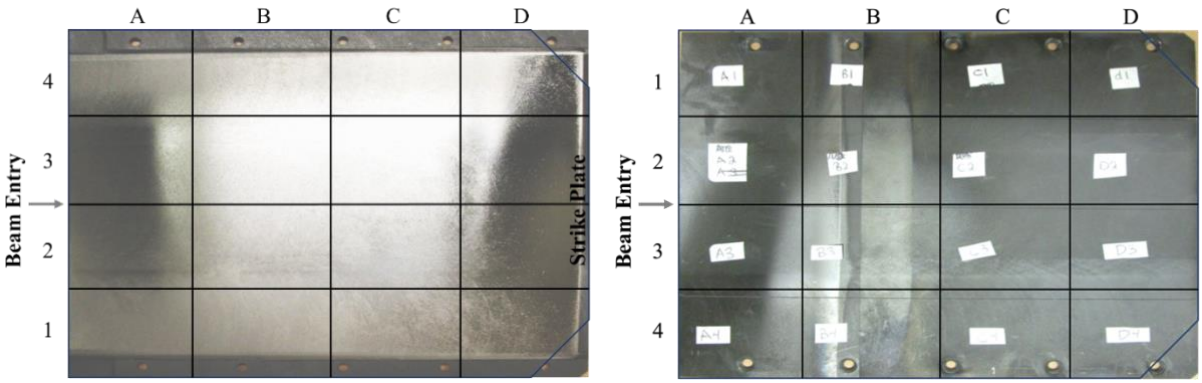

Figure 2. Beam facing side (left) and non-beam facing side (right) of the graphite plate covered in sputtered ions.

The results of this study are reported along with analysis and discussion of the potential deposition mechanism of the Yb layer on the collection and strike plate which differed. It is proposed that directional deposition of Yb ions occurs first in the defect regions of the collection plate. As deposition continues, it leads to the eventual formation of directional globs that elongate and grow into (1) plates, then (2) stacks, and finally (3) sheets of Yb. The ytterbium layer appears to have a definite phase boundary with the graphite layer of the collection plate. It was also determined that during irradiation with the Yb ion beam, sputtered carbon becomes interpolated within the Yb surface layer of the collection plate and has an amorphous microstructure.

2. SEM CHARACTERIZATION

In this study, the surface of the collected ytterbium was captured as 2D maps across the beam and non-beam side of the provided graphite plate, both using the SEM for structural information and the EDS for elemental confirmation. The plate was broken into smaller sections to fit into the different analytical tools' chambers, to make four columns and four rows, shown in Figure 2. SEM images were taken at several spots across the plate's surface along the beam-facing side. The structures visible by SEM appear to be fully mirrored on either side of the center line, including the directionality of the deposition product. In rows 1 and 4, the rough surface of the graphite is visible at the outer edges where the plates were masked by other parts of the collector. Proceeding inward towards rows 2 and 3, the amount of deposition increases significantly, forming a glob region that becomes a plate region made of separate grains, which merge into a stacked region on rows 2 and 3, and, in the center, a sheet region. In addition, proceeding from the beam entry side (A) to the strike plate (perpendicular to the edge of column D), the thickness of the Yb deposition also increases, and the entirety of column D shows the formation of a sheet region," as described in Figure 3.

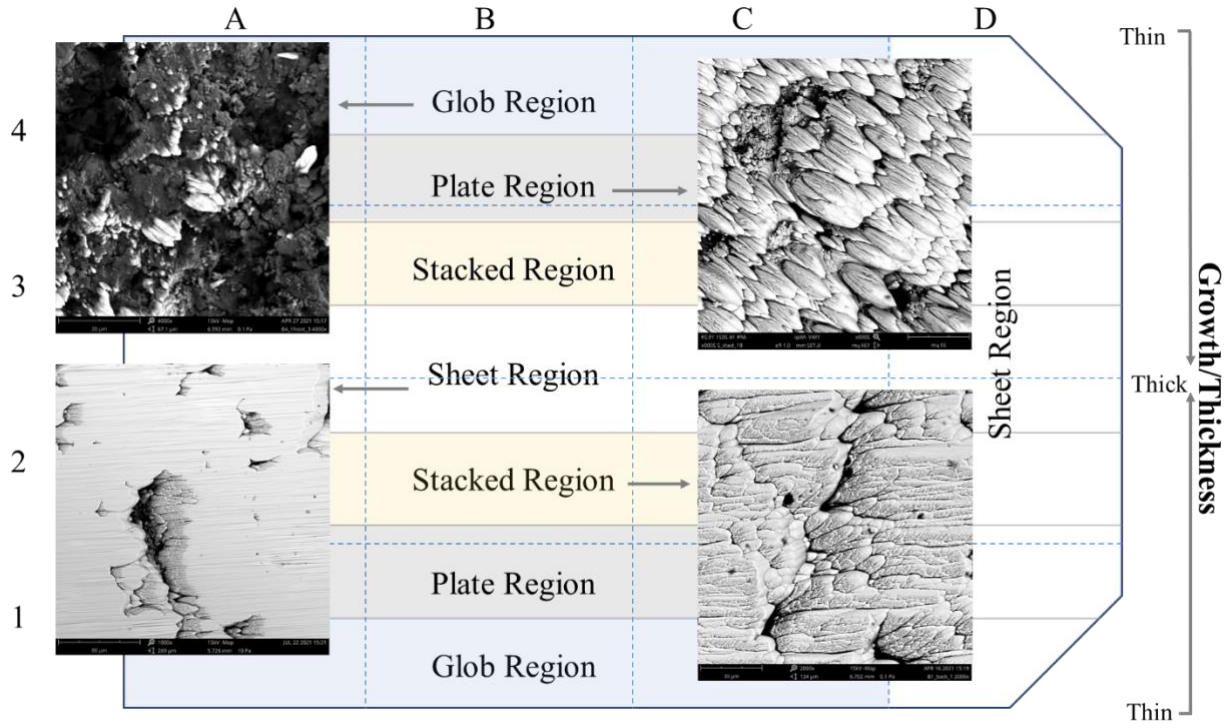

Figure 3. SEM images for distinct plate regions on the collection plate, as determined by the thickness of Yb deposition. All images are at 3,000x magnification.

Through EDS, the structures were confirmed to be Yb, as shown in Figure 4. In this figure, the progression of the Yb deposition from the glob region is seen near the edge of the unexposed graphite on the edge of the plate inward to the sheet region along Column B. Additionally, rough estimates of the atomic concentrations of various other elements were reported. Note, the concentration of Yb is expected to increase from the edge of Row 1 toward the center line. At the centermost point, the concentration of C is still significant, but it is outside the expected ratio for the formation of a coordinating species (e.g., carbonate or carbide), suggesting that the Yb might have trapped sputtered graphite during deposition.

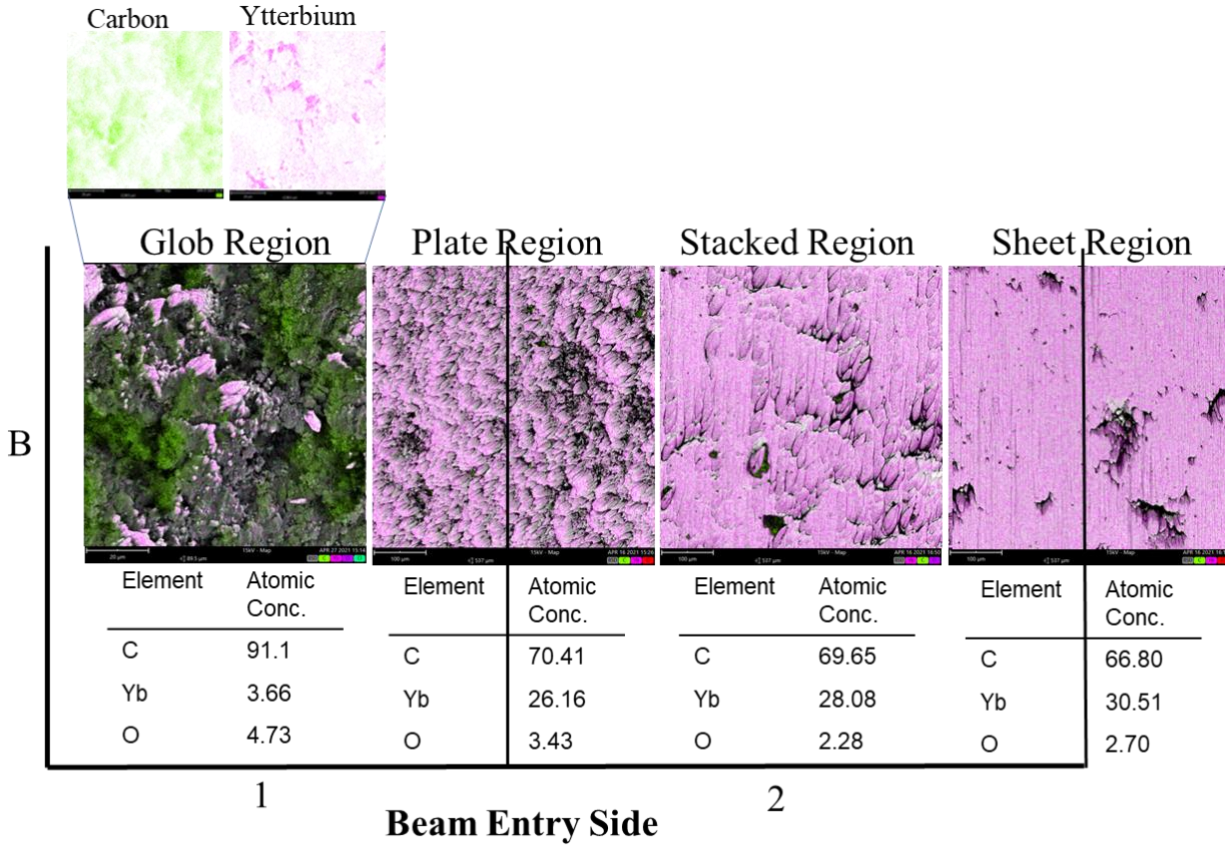

Figure 4. EDS images of the four main regions of deposition on the collection plate, as seen on Column B. The remainder of the column mirrors this pattern, with slight variation in atomic concentrations.

Although the crystallinity of the structures cannot be determined by SEM, a definite, repeatable, and directional pattern begins to emerge in the structures as the amount of material deposited on the surface increases. It is proposed, as shown in Figure 5, that the deposition of Yb begins on rough areas of the graphite. As deposition continues, structures resembling elongated globs begin to form, with a directionality associated with the angle of the sputtered particles [2, 3]. On each of these elongated globs, smaller structures appear in scale-like shapes across the surface. As these globs continue to grow, the globs expand in both diameter and in length, eventually merging into plates [4]. The growth continues and the plates become more defined, stacking on top of each other to cover underdeveloped globs and showing crevasses that run parallel to the Yb beam [5]. If more material is deposited, these plates merge into a uniform sheet with the same feature running parallel from the incident beam path [6].

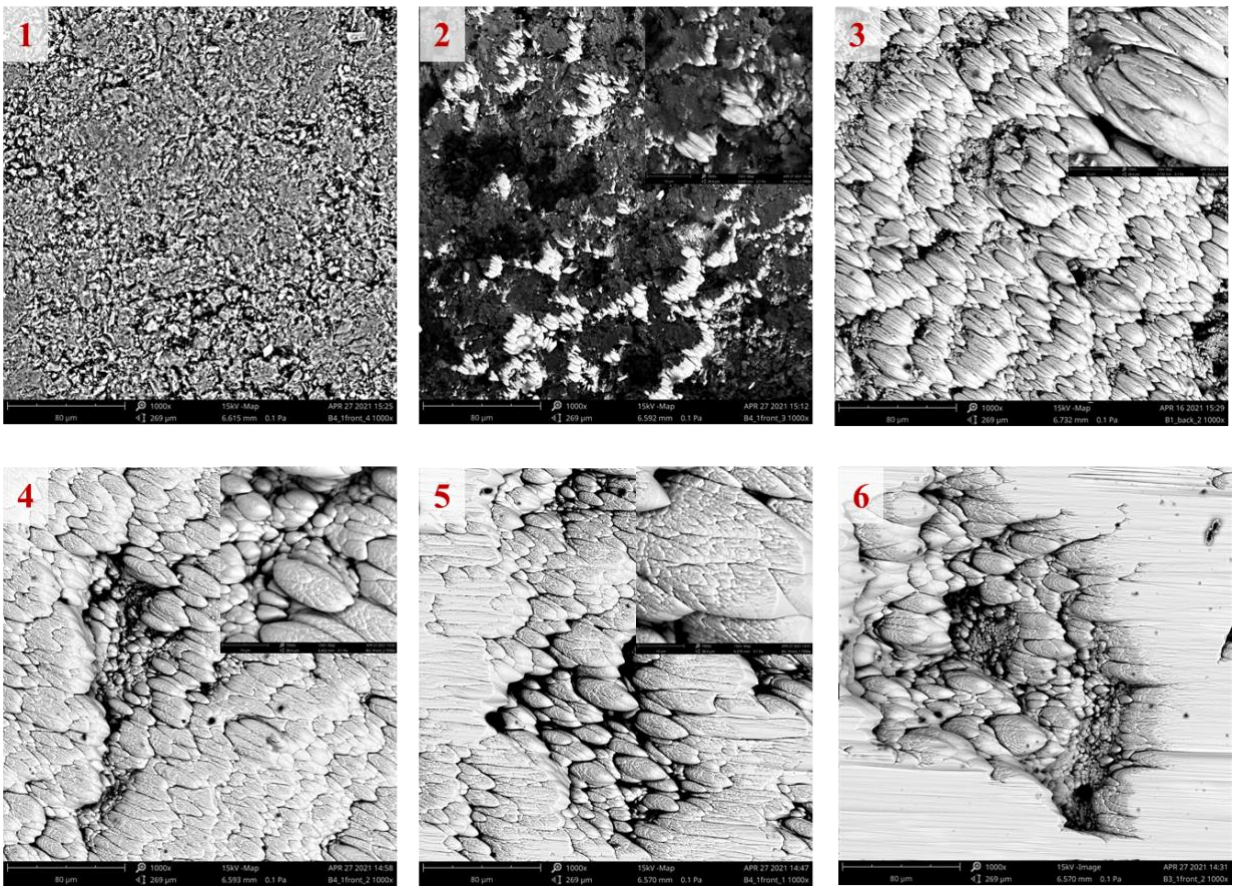

Figure 5. Proposed deposition pattern on the collection plate, with all images at 1,000x and insets at 8,000x to show detail. [1] Unirradiated graphite, [2] formation of globs, [3] elongation of globs into plates, [4] plates beginning to fuse into [5] sheets, and finally [6] an imperfection in an otherwise largely uniform sheet.

Figure 6 reveals a cross section of each of the four major regions—glob [1], plate [2], stacked [3], and sheet [4] regions—that were also examined to get a better insight into the formation of these structures. The Yb appears to collect in the depressed regions of the cross section and elongate outwards and upwards, along the path of the sputtered ions. When the material becomes heavy enough, it merges and folds over itself, creating rows of plates. With time, increased deposition, and heating, the stacked globs fully merge into a single sheet of Yb. Noticeable is a definite phase boundary between the ytterbium layer and the graphite layer.

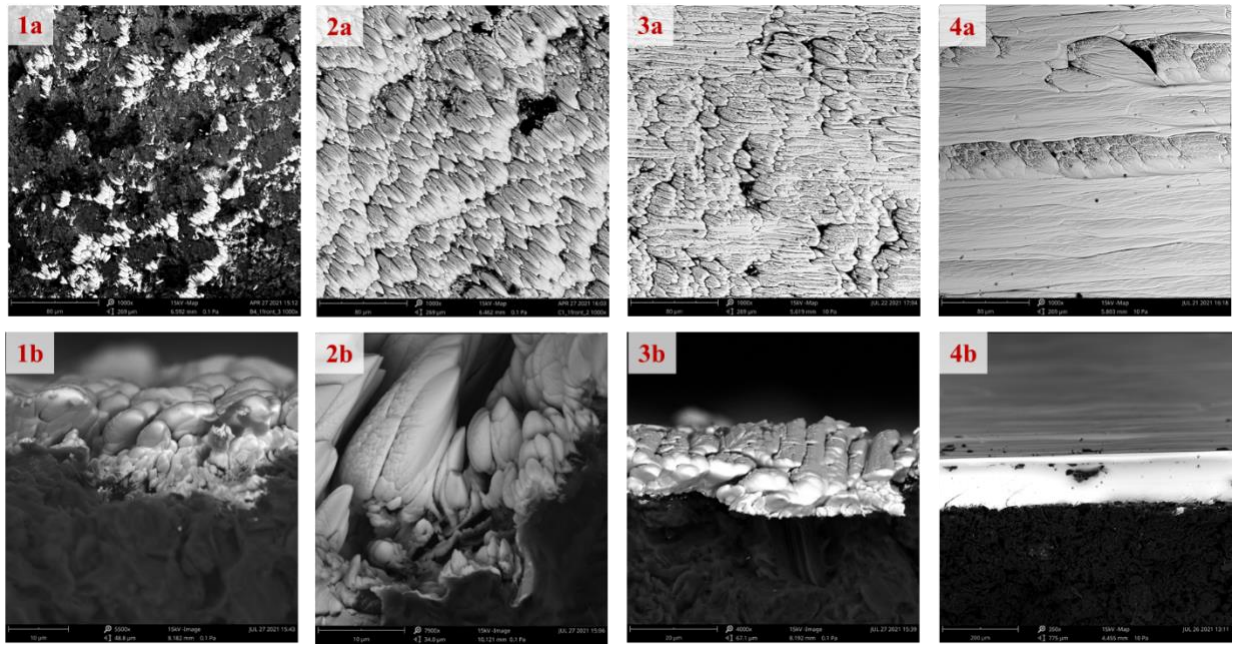

Figure 6. Top view [a] and cross-sectional view [b] of various stages of Yb deposition on the collection plate. [1] Glob region, [2] plate region, [3] stacked region, and [4] sheet region.

The directionality of the globs was associated with the sputter profile of the secondary particle resulting from ion impact on the strike plate. This was determined by the presence and characterization of a small amount of deposition on the non-beam side of the plate, especially on the B column. Figure 7 shows a comparison between the beam side [a] and non-beam side [b] structures. On the non-beam side, the deposition appears to align with the imperfections in the graphite, even including the striations caused by the machining of the graphite. This specific deposition appears to grow into amorphous globs with no directionality and quickly proceed to the sheets stage with striations still visible within those sheets. Additionally, the deposition appears to be made of much smaller formation before proceeding directly into what appears to be a sheet-like region, rather than stacking before proceeding into sheets. Although further research is needed to confirm this hypothesis, it is concluded that this type of deposition is most likely a result of evaporation and recondensation of Yb.

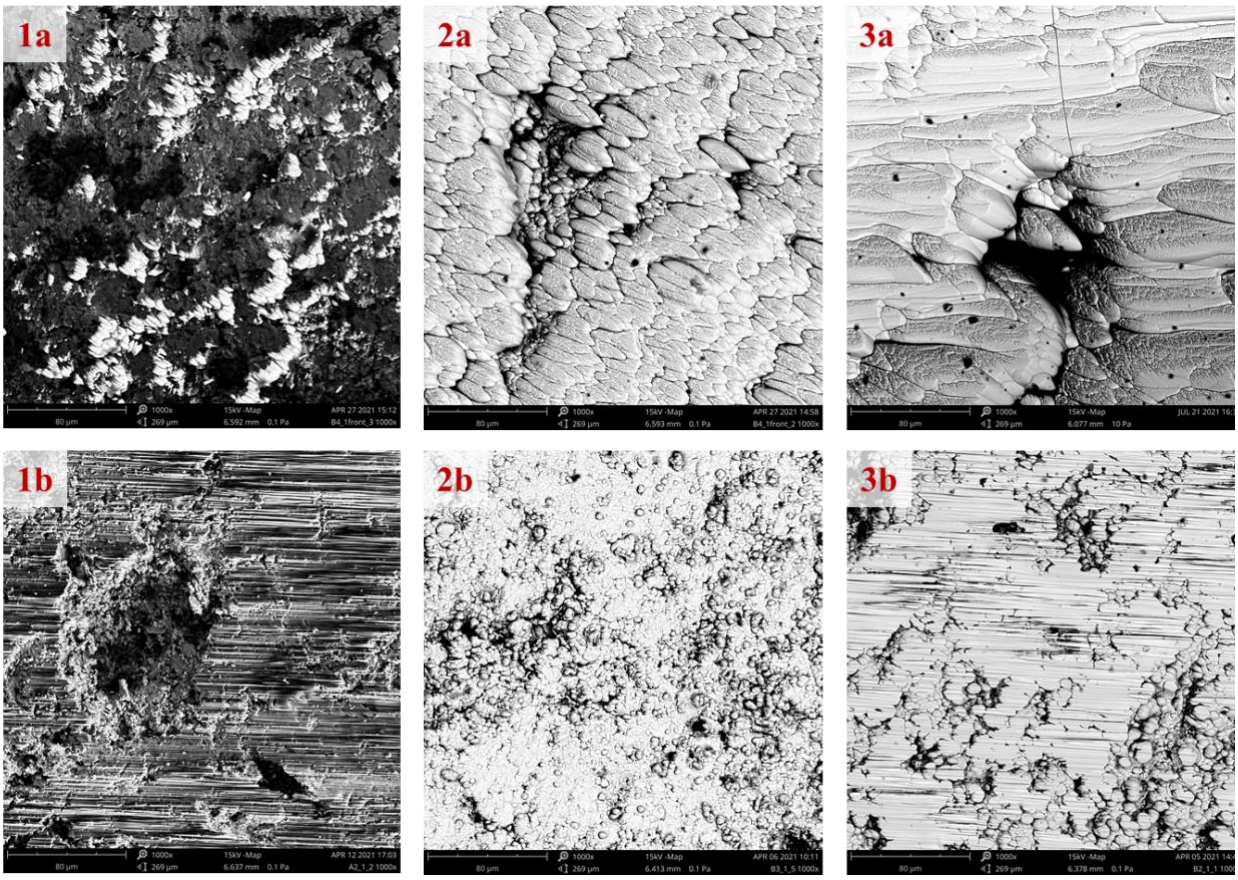

Figure 7. The beam side [a] and non-beam side [b] depositions of Yb at the glob [1], plate [2], and stacked [3] stages of deposition on the collection plate.

Characterization of the strike plate also yielded insight into the effects of incident beam impact and subsequent sputtering. The results from these events, seen in Figure 1, included ion milling[5] of the graphite in the beam strike region of the plate and Yb deposition. An ion milling gradient was observed across the strike plate with more pronounced milling features near the center (column C), and fewer features near the edges (columns A and E). This pattern was reversed for Yb deposition since more deposition occurred near the outside (columns A and E) and less at the center (column C) of the strike plate. However, the Yb deposition gradient was more evident in SEM images of the strike plate. The strike plate can be described as having four regions, Figure 8. These regions include [1] the center of the beam strike, the intermediate beam strike [2], the edge of the beam strike [3], and the outside of the beam strike [4]. At the center region [1], voids and individual graphite sheets were distinguishable due to ion milling, and very little Yb was observed.[7, 8] In the intermediate region of the beam strike [2], the exposed graphite sheets were still visible but with a Yb coating. Moving toward the edge region of the beam strike [3], the Yb layer is thicker and has some smoothness, the graphite sheets are less distinguishable, and the void areas are more pronounced. Outside the beam strike region [4], the Yb layer was the thickest and smoothest but had several voids. In summary, in the non-heavily milled regions, the metal appeared to be fused by melting and was smooth. There were several voids in heavily milled regions, and the individual graphite sheets were clearly visible with decreasing amounts of Yb. Note that the ion milling patterns observed in the regions numbered 1–4 in Figure 8 were not observed on collection plate images.

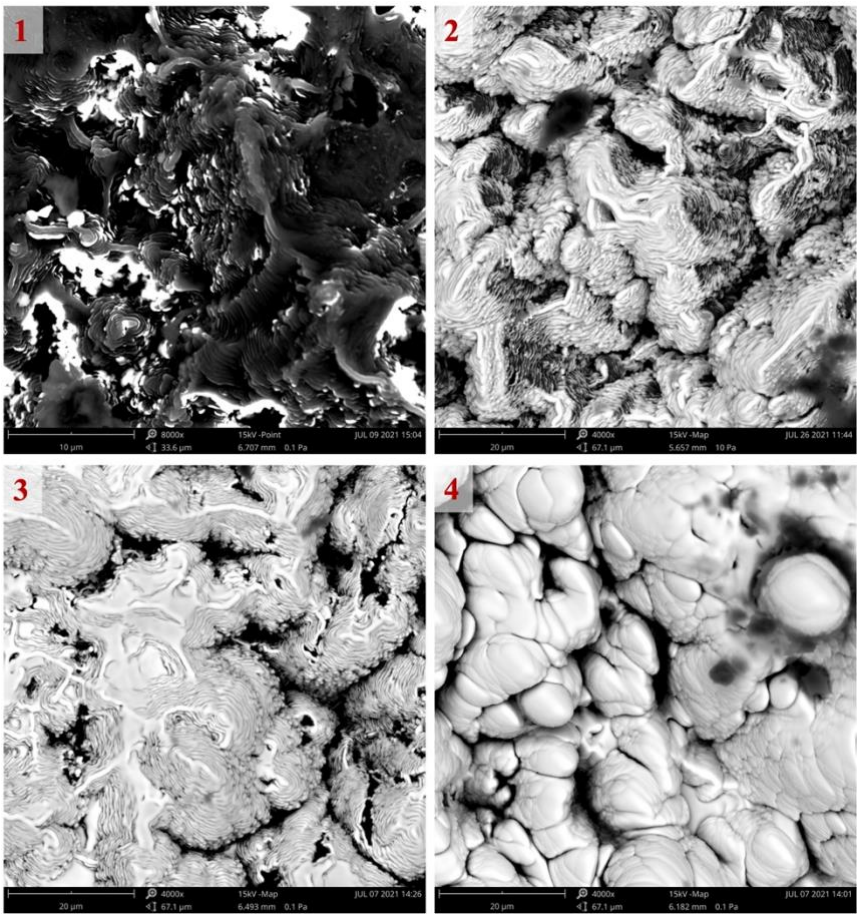

Figure 8. SEM images of the four regions observed on the strike plate after ytterbium ion beam irradiation. The images show the four regions: center of the beam [1], intermediate beam [2], edge of the beam [3], and outside of beam strike [4].

3. XPS CHARACTERIZATION

XPS characterization enables analysis of the surface chemistry of the plates before and after Yb ion beam irradiation. This technique allows for a detailed study of the surface atomic composition, oxidation state, reactivity, and structure of a substrate.[9-11] To identify changes in the surface chemistry of the graphite after Yb ion beam irradiation, XPS spectra were acquired of samples from a pristine graphite plate, a collection plate, and a strike plate. Each sample was irradiated at multiple positions with x-ray photons as seen in Figure 9. Wide energy surveys (see Figure 10Figure 10) were collected from pristine, strike, and collection plate samples to determine surface composition. Pristine graphite samples had binding energy peaks in the valence band region at ~25 eV, a C 1s peak at 284.5 eV, and a C-KVV Auger peak at 1225 eV. A trace amount of O at 532.4 eV was also observed on the surface of the pristine sample, which was most likely absorbed from the atmosphere. After Yb ion beam irradiation, Yb was observed on the surface of the collection and strike plate samples at ~187 eV, and in the valance bond region, see Figure 10. Ion beam irradiation also resulted in a decrease in the carbon surface composition and a significant increase in the O surface composition (see Table 1). The surface composition of O differs from the atomic concentration determined by EDS. This difference emphasizes the uniqueness and analysis depth of each technique. As EDS depth of characterization is greater than that of XPS, thereby suggesting that O is mostly a surface species and has low diffusivity into the Yb layer. The increase in O surface composition is likely associated with the Yb and C surface species being highly reactive after ion beam treatment and upon exposure to atmospheric air. Thus, spectral features representing Yb metal and Yb oxide were expected. If Yb oxide was the sole species on the surface, the O/Yb composition ratio would be ~1.5. However, the composition ratio falls closer to that of Yb carbonate (with a 4.5 O/Yb ratio) as experimental values range from 4.9–5.2 and 4.3–5.7 on the collection and strike plates, respectively. This could in fact be a mixture of Yb carbonate and Yb oxide. To better understand these surface species on the collection and strike plates, a detailed study of the individual Yb, O, and C peaks was carried out by acquiring core level electron spectrum of these peaks.

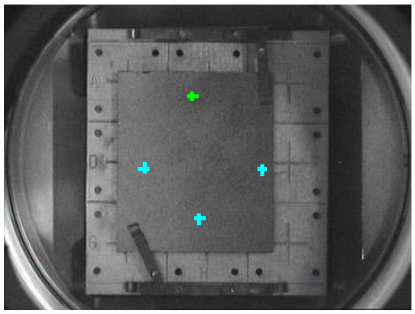

Figure 9. Sample C3 from a graphite plate with Yb collected on it. The sample surface chemistry was studied by irradiating with x-rays at four positions on the samples**.**

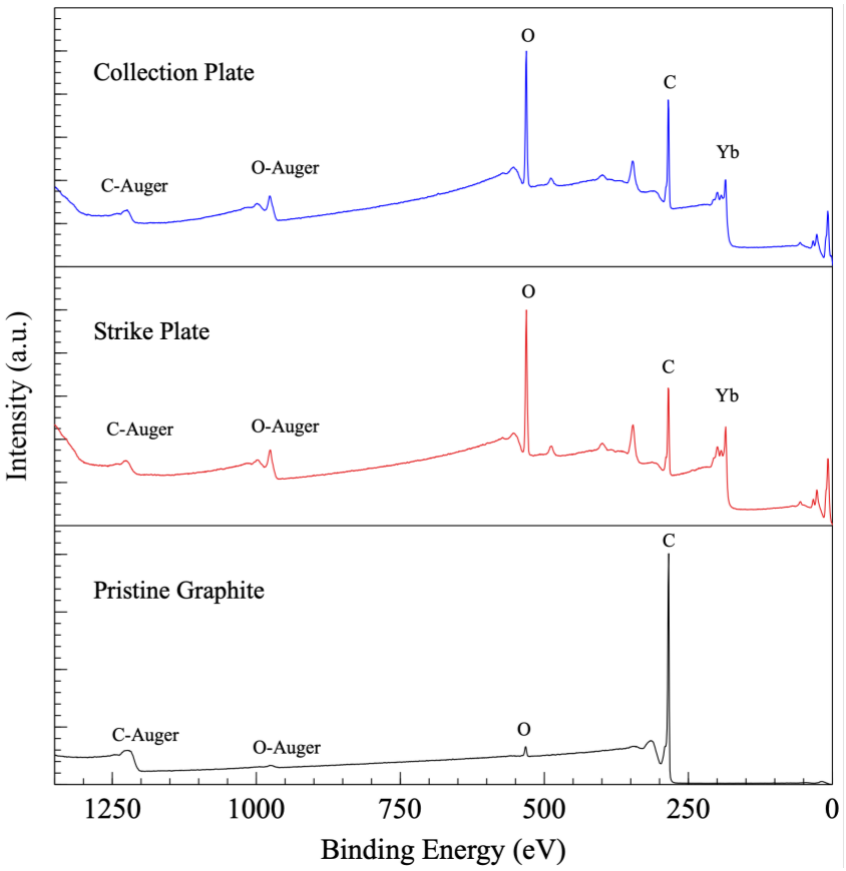

Figure 10. Wide energy range survey spectra of collection (blue) and strike (red) plate samples compared with pristine graphite plate sample (control, black). These spectra are representatives of other collection or strike plate samples.

Table 1. Surface composition (%) of C, O, and Yb on surface of pristine graphite, strike, and collection plate samples.

Pristine[a] samples	Yb	O	C	Si[b]	F[b]	Na[b]	O/Yb
A		2.15	97.85				
B		2.15	97.78	0.08			
C		2.17	97.83				
D		2.05	97.95				
Strike[a] samples	**Yb**	**O**	**C**	**Si[b]**	**F[b]**	**Na[b]**	**O/Yb**
A	5.70	29.52	64.15	0.37	0.20	0.08	5.20
B	8.75	39.02	52.15	0.08			4.47
C	8.43	37.83	53.73				4.49
D	8.25	38.07	53.37	0.17	0.17		4.61
E	4.57	25.18	69.92	0.22	0.15	0.12	5.52
Collection[a] samples	**Yb**	**O**	**C**	**Si[b]**	**F[b]**	**Na[b]**	**O/Yb**
A	6.28	32.57	61.15				5.18
B	6.22	31.76	62.04				5.11
C	6.13	31.74	62.14				5.18
D	6.25	30.69	56.27	0.28			4.91

[a]Samples A, B, C, D, and E represent the average data collected from samples in columns A, B, C, D, or E.
[b]Other trace elements observed on the surface of the graphite plate samples.

Analysis of the Yb 4d electron peak yielded more insightful details of the surface species observed after Yb ion beam exposure and the oxidation state of the Yb. Figure 11 shows ytterbium 4d core-level electron spectra for collection and strike plate samples. To aid in determining the Yb oxidation state, these spectra were superimposed over reference spectra taken from Padalia et al. study of Yb metal, Yb-partially oxidized, and Yb oxide (Yb^{+3}).[12] Comparison of these spectra with the literature confirmed that the surface Yb in these samples is predominately in the +3 oxidation state as their peak shape closely resembled that of Yb oxide. Element surface composition calculations seemed to indicate that Yb carbonate could be present. Indeed, it may be present, because in both Yb_2O_3 and $Yb_2(CO_3)_3$, the Yb is in the +3 state. Therefore, the spectra could likely represent a mix of Yb oxide and Yb carbonate, as their spectra could potentially have similar peak shape. No reference spectrum of $Yb_2(CO_3)_3$ was found in the literature. The shoulder on the low binding energy side indicates a reduced form of Yb as compared to Yb^{+3}. It is likely a small amount of metallic Yb because Yb^{+2} is not a highly stable form.

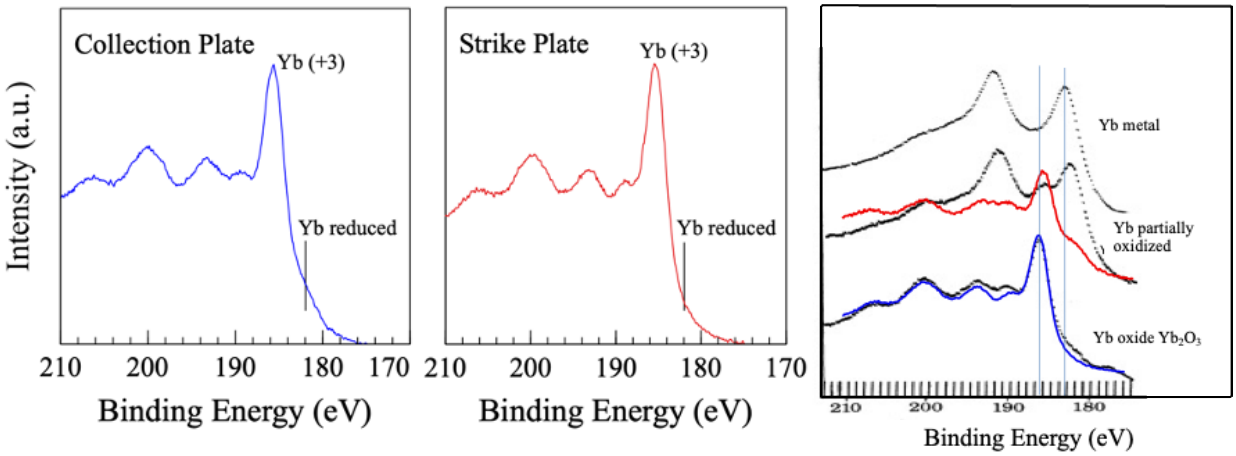

Figure 11. Yb 4d core-level electron spectra from collection (sample C2) and strike (sample A2) plate samples (left and middle). The strike plate spectra have been superimposed over reference spectra taken from the literature for comparison (right). These spectra are representative of data collected from all collection or strike plate samples.

The O 1s core-level spectra for pristine graphite, strike, and collection plate samples are shown in Figure 12. These spectra demonstrated a change in the surface species after irradiation of the strike and collection plates with the Yb ion beam when compared with the pristine graphite samples. For example, the pristine graphite samples revealed an O 1s peak at 532.48 eV with comparable contribution from two main bond types: O=C bond assigned at ~531 eV and O–C bond centered at ~533 eV (see fits in Figure 12)[11]. After exposure to the Yb ion beam, the O 1s peak shifted to lower binding energy at 531.68 eV and at 531.98 eV for both the strike and collection plate samples, respectively. The shift was due to an increase in the O=C group on the surface of the samples, thereby leading to increased contribution of the O=C bond type in comparison with other bond types in the O 1s peak. The shift might be indicative of the surface chemistry such as carbonate, absorbed carbon dioxide, and graphite oxide species on and within the surface of the Yb layer. The contribution of an O–Yb bond type was also observed as a small shoulder on the low binding energy side of the collection and strike plate spectra. This is further support of Yb oxide or carbonate species on the surface.

The C 1s peaks were also affected by Yb ion beam irradiation. The pristine graphite C 1s spectra had a C–C peak at 284.5 eV with mostly C(sp^2) bond type (see Figure 12). After exposure to the Yb ions, the C–C peak shifted from being mostly composed of sp^2 carbon to an increased amount of sp^3 carbon character at ~285 eV. This was observed in both strike and collection plate spectra (see Figure 12). The increase in C(sp^3) character suggests the microstructure of the carbon on the surface had changed as a result of the irradiation and collection process.[13, 14] Also observed on the higher binding energy side of the C–C peak was C–O bond type at 286.5 eV, O=C–O bond type at 288.7 eV, and carbonate bond type at 289.8 eV. The appearance of the carbonate peak in the C 1s spectra further supports the existence of Yb carbonate on the surface.

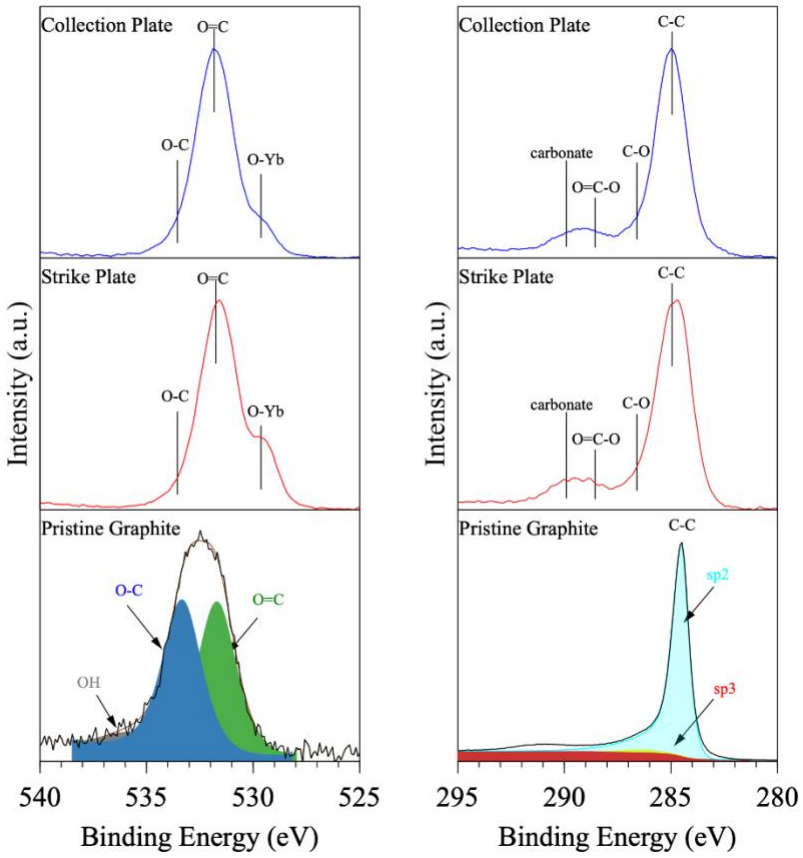

Figure 12. O 1s and C 1s core-level electron spectra regions taken of pristine graphite, strike plate, and collection plate samples. Plots on the left are of O 1s peaks, and plots on the right are of C 1s peaks. These spectra are representatives of most spectra taken from all collection plate, strike plate, and pristine graphite samples, respectively.

As evident from the analysis above, after exposure to the Yb ion beam, the structure of the carbon observed on the surface of the collection and strike plates was no longer primarily graphite but exhibited some amorphous character. The shift toward sp^3 carbon bond type on the surface of the strike and collection plate samples is supported by d-parameter data. This parameter has been shown to be highly sensitive to changes in carbon hybridizations. For example, pure diamond, which is composed of amorphous C(sp^3), typically has a d-parameter of 13 eV. While pure graphite, fully crystalline sp^2 carbon, has a d-parameter of 24 eV. The derivative spectra for pristine graphite and collection samples had d-parameters of 21.6 eV and 14.2 eV, respectively (see Figure 13). Therefore, after irradiation with the Yb ion beam, the carbon on the surface of the Yb layer had characteristics of amorphous C(sp^3). It is feasible that the sp^3 carbon observed is from sputtered carbon particles from the strike plate interpolated in the growing Yb layer on the collection plate. This conclusion can be supported by physical ion milling patterns observed on the strike plate caused by the ion beam (Figure 1). Similar ion milling patterns were observed in SEM images of the strike plate, in Figure 8. However, the collection plate, which was not directly impacted by the ion beam, did not have ion milling patterns. Furthermore, there was a particular area examined on the collection plate where Yb could not be collected, nor did it have direct exposure to the ion beam. This area had a d-parameter of 18.7 to 20 eV. Thus, the transition from sp^2 to sp^3 carbon under these environmental conditions was partially an artifact of the ion beam or sputtering and not a result of the thermal radiation created by those events. This would suggest that the bulk graphite layer underneath the Yb layer may still be crystalline. Cross-sectional SEM images (Figure 6) of the collection

plate exemplified that the Yb and graphite appear to be distinct layers, which further suggest the graphite beneath the Yb layer might still have a high degree of graphitization.

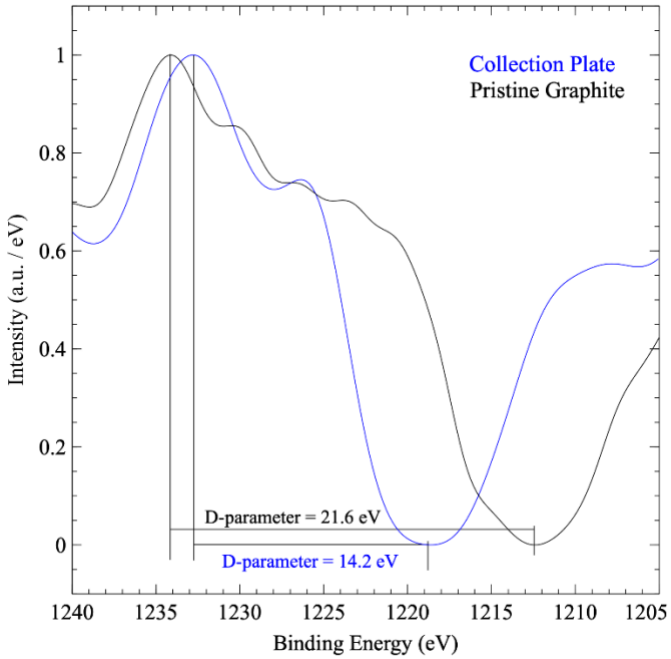

Figure 13. The collection plate and pristine graphite d-parameters, which are measured from the difference between the maximum and minimum of the first derivative of the C-KVV Auger peak. The plots shown are representatives of all collection and graphite plate samples.

4. RAMAN CHARACTERIZATION

Microstructural changes in graphite upon irradiation with ions, electrons, or particles can be observed through Raman spectroscopy.[13, 15-17] This technique has been widely used to study structural changes and to qualitatively analyze defects and disorder in carbon materials.[18-21] Thus, Raman is ideal for studying structural changes in graphite samples irradiated with an Yb ion beam. A typical Raman spectrum of crystalline graphite or amorphous carbon has characteristic peaks associated with vibrational modes of the carbon bond. The peak position, intensity, width, and area have been shown to correlate to the microstructure of the material.[20, 22-25] Furthermore, valuable information about the crystallite size and dimension, defect types, hybridization character, degree of structural defects, and structural transformation can also be derived from spectral analysis. For graphite, the most prominent peaks that are important to this analysis and discussion are the D and G band peaks.[8, 26] In a crystalline graphite spectrum, the G band peak at ~1580 cm^{-1} represents a first-order sp^2 carbon vibrational mode within the graphite plane, and the smaller D band peak at ~1350 cm^{-1} is attributed to defects or disorder within the graphite structure. While in a typical amorphous carbon spectrum, the D and G band peaks are shifted and broaden in comparison with their analogous peaks in the crystalline graphite spectrum.

Pristine graphite, strike plate, and collection plate samples were excited with a laser at 532 nm, and their Raman spectra are shown in Figure 14. Spectral features for crystalline and amorphous carbon were observed before and after the Yb ion beam irradiation. All peak positions were determined by peak fitting using the Lorenzo method. The pristine graphite spectrum resembled crystalline graphite with the G and D band peaks at 1577 and 1347 cm^{-1}, respectively. However, the irradiated sample spectra had spectral features comparable to amorphous carbon. In the case of the strike plate, the D and G band peaks had broadened and were coalescing, while the D and G peaks from the collection plate sample had coalesced. The strike plate and collection plate samples' D band peaks, observed at 1360 and 1343 cm^{-1} respectively, were larger than the analogous peak in the pristine sample spectrum and were shifted. This shift indicates an increase in structural defects within the graphite plane induced by Yb ion beam radiation. These defects are likely vacancies in the crystalline lattice induced by carbon sputtering and disordered carbon vibrational modes from ion impact.[5, 27] The strike and collection plate G band peaks had also shifted to lower wave numbers, 1557 and 1525 cm^{-1}, respectively, revealing a structural transformation. Based on the amorphization model proposed by Ferrari et al., shifts in the G peak position reveal information on a carbon material's microstructure.[22, 25, 28] Using this model would suggest the microstructure of the strike plate samples had transitioned from graphite to nanocrystalline graphite. While the microstructure of the collection plate samples had transitioned even further toward an amorphous carbon structure with some sp^3 carbon defects. Lastly, a new band was observed in the collection and strike plate spectrum with a peak at ~640 cm^{-1} (see Figure 14). This peak—and others that would be expected below 500 cm^{-1}—are associated with the vibration modes of Yb–C or Yb–O bonds that occur below 800 cm^{-1}.[29]

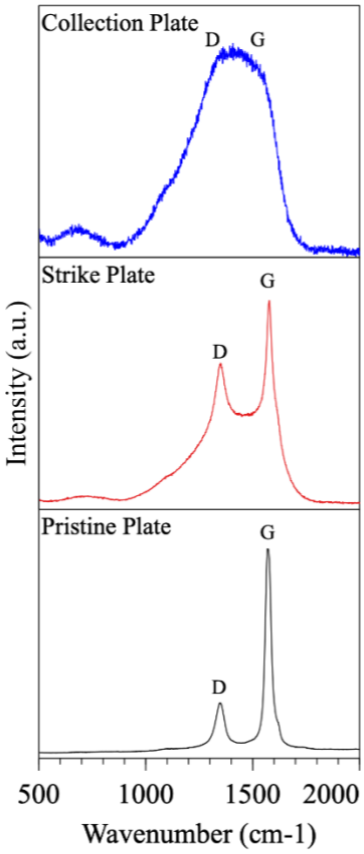

Figure 14. Representative spectra of all the pristine graphite, strike, and collection plates samples analyzed.

Analysis of the D and G peak areas and intensity values also support microstructural changes observed in strike and collection plate samples that were induced by Yb ion irradiation. The relative intensity ratio between D and G bands, I_D/I_G, is considered a good parameter for estimating the degree of graphitization of carbon material.[22, 25] The D and G band peak intensities, areas, and ratios were determined by the Lorentzian curve fitting (see Table 2). Pristine graphite had an I_D/I_G ratio of 0.22. Upon exposure to the Yb ion beam, the ratio increased to 1.11–1.96 for both the strike and collection plate samples. The post-Yb irradiation ratios suggested that the carbon's structure was likely nanocrystalline graphite, according to the amorphization model.[22, 25] Disruption in the long-range graphite crystalline structure causing a nanocrystalline graphite structure was attributed to in-plane defects (e.g., vacancies and deformed sp^2 hybridized bonds) that are consequences of ion bombardment and carbon sputtering. Further evidence supporting a structural transition after Yb ion irradiation was observed in the in-plane crystallite size, L_a,[24, 30, 31] calculated from Tuinstra and Koenig equation[32] ($I_D/I_G = C(\lambda)/L_a$). Table 2 shows that the crystallite size was significantly smaller in the Yb irradiation samples. These results indicate that the microstructure of the strike and collection plate samples were no longer graphite after Yb ion irradiation but nanocrystalline graphite and possibly amorphous carbon as indicated by the transition of the G band peak position. However, based on SEM images and XPS data, the carbon vibrational modes observed in the collection and strike plate spectra were most likely from carbon interpolated within the collected Yb layer (with a thickness of 10 to over 150 µm) and not from the graphite layer beneath the collected Yb layer. This assessment is based on the thickness of the Yb layer in comparison with the depth of the characterization method that is on the nanometer scale.

Table 2. Calculation of peak position, intensity ratio, area, area ratio, and crystallite size.

Sample[a]	D position (cm^{-1})	G position (cm^{-1})	I_D/I_G Max height	A_D FWHM[b]	A_G FWHM	A_D/A_G FWHM	L_a (nm)
Pristine	1347	1577	0.22	57.5	29.6	2.01	37.32
Collection plate							
A	1341	1522	1.44	288.7	143.5	2.01	3.44
B	1344	1528	1.43	311.5	139.3	2.23	3.45
C	1344	1525	1.55	291.7	139.7	2.09	3.22
D	1342	1523	1.53	293.5	142.5	2.06	3.24
Strike plate							
A	1363	1558	1.22	329.4	83.2	5.54	5.82
B	1364	1549	1.43	328.2	130.9	2.51	3.48
C	1367	1570	1.11	289.6	83.8	3.54	5.03
D	1372	1568	1.36	322.9	94.0	3.47	3.70
E	1346	1541	1.96	389.4	124.7	3.15	2.56

[a]Samples A, B, C, D, and E represent the average data collected from samples in columns A, B, C, D, and E, respectively.
[b]FWHM=full width at half maximum.

5. CONCLUSION

This report discusses findings from surface characterization of graphite parts used in the EMIS for collection of enriched isotopes. The EMIS is used to separate and enrich isotopes, in this case, Yb. As the Yb ion beam travels within the device, the isotopes are separated and then collected. Collection of isotopes proceeds by ion beam impact on a graphite strike plate, which induces sputtering of Yb and C particles. The particles are collected on adjacent collection plates, also made of graphite. The results of the ion beam impact on the strike plate and sputter particles impact on the collection plates can be observed and analyzed by surface characterization techniques. In this study, SEM, XPS, and Raman were used to understand changes induced on graphite plates by Yb ion beam irradiation. With these methods, Yb was confirmed as a surface species found as Yb oxide and Yb carbonate. Analysis of SEM images suggests that Yb deposition is a unique process with a specific deposition mechanism on the collection plate that differs from the strike plate. It is proposed that directional deposition of Yb ions occurs first in the defect regions of the collection plate. As deposition continues, it leads to the eventual formation of directional globs that elongate and grow into (1) plates, then (2) stacks, and finally into (3) sheets of Yb. The ytterbium layer appears to have a definite phase boundary with the graphite layer. It was also determined that during irradiation with the Yb ion beam, the sputtered carbon becomes interpolated in the growing Yb surface layer on the collection plate and has an amorphous microstructure, which was confirmed through Raman and XPS characterization. Ion beam impact on the strike plate caused ion milling, which was the most severe in the middle of the beam strike region. Where heavy ion milling was observed, there was also less Yb. However, areas with no heavy ion milling showed a relatively larger amount of annealed Yb. Overall, from this analysis it is concluded that Yb poorly interacts with amorphous and graphitic C of the strike and collection plates, as by the lack of an observable interfacial layer. This suggest that Yb will be poorly bound to the graphite. This understanding will be useful when designing future materials for the collection plate that allow better control of the substrate and enriched isotope interaction.

6. REFERENCES

1. Love, L. O., Electromagnetic Separation of Isotopes at Oak Ridge. *Science* **1973,** *182* (4110), 343-352.
2. Hart, K. J. In *Development of a Pilot Scale Facility for Production of Enriched Stable Isotopes*, The International Chemical Congress of Pacific Basin Societies, Honolulu, Hawaii, Honolulu, Hawaii, 2015.
3. Egle, B. J.; Hart, K. J.; Aaron, W. S., Stable Isotope Enrichment Capabilities at Oak Ridge National Laboratory. *Journal of Radioanalytical and Nuclear Chemistry* **2014,** *299*, 995-999.
4. Energy, U. D. o., Meeting Isotope Needs and Capturing Opportunities for the Future: The 2015 Long Range Plan for the DOE-NP Isotope Program. Energy, U. D. o., Ed. Washington, DC, 2015.
5. Coratger, R.; Claverie, A.; Chahboun, A.; Landry, V.; Ajustron, F.; Beauvillain, J., Effects of ion mass and energy on the damage induced by an ion beam on graphite surfaces: a scanning tunneling microscopy study. *Surface Science* **1992,** *262*, 208-218.
6. Appy, D.; Lei, H.; Wang, C.-Z.; Tringides, M. C.; Liu, D.-J.; Evans, J. W.; Thiel, P. A., Transition metals on the (0 0 0 1) surface of graphite: Fundamental aspects of adsorption, diffusion, and morphology. *Progress in Surface Science* **2014,** *89* (3-4), 219-238.
7. Habenicht, S.; Bolse, W.; Lieb, K. P., Nanometer ripple formation and self-affine roughening of ion-beam-eroded graphite surfaces. *PHYSICAL REVIEW B* **1999,** *60* (4), 2200-2203.
8. Habenicht, S., Morphology of graphite surfaces after ion-beam erosion. *Physical Review B* **2001,** *63* (12).
9. Gouder, T.; Colmenares, C. A.; Naegele, J. R., A surface spectroscopy study of U overlayers on graphite. *Surface Science* **1995,** *342* (1-3), 299-306.
10. Marcus, P.; Hinnen, C., XPS study of the early stages of deposition of Ni, Cu and Pt on HOPG. *Surface Science* **1997,** *392*, 134-142.
11. Buttner, M.; Oelhafen, P., XPS study on the evaporation of gold submonolayers on carbon surfaces. *Surface Science* **2006,** *600* (5), 1170-1177.
12. Padalia, B. D.; Lang, W. C.; Norris, P. R.; Watson, L. M.; Fabina, D. J., X-Ray Photoelectron Core-Level Studies of the Heavy Rare-Earth Metals and Their Oxides. *Proceedings of the Royal Society of London. Series A, Mathematical and Physical Sciences* **1977,** *354* (1678), 269-290.
13. Ravesi, S.; Terrasi, A.; Torrisi, L.; Foti, G., Electronic structure of 0.5 keV Ar^+ irradiated graphite. *Radiation Effects and Defects in Solids* **1993,** *127* (2), 137-145.
14. Büttner, M.; Reinke, P.; Oelhafen, P., UV photoemission study on fullerene molecules deposited on defect-rich carbon surfaces. *Surface Science* **2007,** *601* (1), 280-286.
15. Archanjo, B. S.; Maciel, I. O.; Ferreira, E. H.; Peripolli, S. B.; Damasceno, J. C.; Achete, C. A.; Jorio, A., Ion beam nanopatterning and micro-Raman spectroscopy analysis on HOPG for testing FIB performances. *Ultramicroscopy* **2011,** *111* (8), 1338-42.
16. Bardotti, L.; Prevel, B.; Trexilleux, M.; Melinon, P.; Perez, A., Deposition of preformed gold clusters on HOPG and gold substrates: influence of the substrate on the thin film morphology. *Applied Surface Science* **2000,** *164*, 52-59.
17. Bertolo, A. A.; Cánneva, A.; Donadelli, J. A.; Gaviola, P. A.; Kreiner, A. J.; del Grosso, M. F., Manufacture, characterization and proton irradiation effects of 12C and 13C thick targets. *Journal of Materials Science* **2021,** *56* (11), 6997-7007.
18. Ferrari, A.; Basko, D. M., Raman spectroscopy as a versatile tool for studying the properties of graphene.
19. Matthews, M. J.; Pimenta, M. A.; Dresselhaus, G.; Dresselhaus, M.; Endo, M., Origin of dispersive effects of the Raman D band in carbon materials. *Physical Review B* **1999,** *59* (10), 6585-6588.
20. Cancado, L. G.; Jorio, A.; Ferreira, E. H.; Stavale, F.; Achete, C. A.; Capaz, R. B.; Moutinho, M. V.; Lombardo, A.; Kulmala, T. S.; Ferrari, A. C., Quantifying defects in graphene via Raman spectroscopy at different excitation energies. *Nano Lett* **2011,** *11* (8), 3190-6.

21. Xu, Z.; He, Z.; Song, Y.; Fu, X.; Rommel, M.; Luo, X.; Hartmaier, A.; Zhang, J.; Fang, F., Topic Review: Application of Raman Spectroscopy Characterization in Micro/Nano-Machining. *Micromachines (Basel)* **2018,** *9* (7).
22. Ferrari, A. C.; Robertson, J., Interpretation of Raman spectra of disordered and amorphous carbon. *Physical Review B* **2000,** *61* (20), 14095-14107.
23. Yang, D.-Q.; Sacher, E., s–p Hybridization in highly oriented pyrolytic graphite and its change on surface modification, as studied by X-ray photoelectron and Raman spectroscopies. *Surface Science* **2002,** *504*, 125-137.
24. Lucchese, M. M.; Stavale, F.; Ferreira, E. H. M.; Vilani, C.; Moutinho, M. V. O.; Capaz, R. B.; Achete, C. A.; Jorio, A., Quantifying ion-induced defects and Raman relaxation length in graphene. *Carbon* **2010,** *48* (5), 1592-1597.
25. Lee, B.-J.; Shin, D.-H.; Lee, S.; Jeong, G.-H., Revealing impact of plasma condition on graphite nanostructures and effective charge doping of graphene. *Carbon* **2017,** *123*, 174-185.
26. Wang, Y.; Alsmeyer, D. C.; McCreeery, R. L., Raman spectroscopy of carbon materials structural basis of observed spectra. *Chemical Material* **1990,** *2* (5), 557-563.
27. Nordlund, K.; Keinonen, J.; Mattila, T., Formation of Ion Irradiation Induced Small-Scale Defects on Graphite Surfaces. *Physical Review Letters* **1996,** *77* (4), 699-702.
28. Ferrari, A. C., Raman spectroscopy of graphene and graphite: Disorder, electron–phonon coupling, doping and nonadiabatic effects. *Solid State Communications* **2007,** *143* (1-2), 47-57.
29. Cui, J.; Hope, G. A., Raman and Fluorescence Spectroscopy of CeO2, Er2O3, Nd2O3, Tm2O3, Yb2O3, La2O3, and Tb4O7. *Journal of Spectroscopy* **2015,** *2015*, 1-8.
30. Cançado, L. G.; Takai, K.; Enoki, T.; Endo, M.; Kim, Y. A.; Mizusaki, H.; Jorio, A.; Coelho, L. N.; Magalhães-Paniago, R.; Pimenta, M. A., General equation for the determination of the crystallite size La of nanographite by Raman spectroscopy. *Applied Physics Letters* **2006,** *88* (16).
31. Cançado, L. G.; Jorio, A.; Pimenta, M. A., Measuring the absolute Raman cross section of nanographites as a function of laser energy and crystallite size. *Physical Review B* **2007,** *76* (6).
32. Tuinstra, F.; Koenig, J. L., Raman Spectrum of Graphite. *J Chem Phys* **1970,** *53* (3), 1126-1130.
33. Merlen, A.; Buijnsters, J.; Pardanaud, C., A Guide to and Review of the Use of Multiwavelength Raman Spectroscopy for Characterizing Defective Aromatic Carbon Solids: from Graphene to Amorphous Carbons. *Coatings* **2017,** *7* (10).

APPENDIX A. EXPERIMENTAL SECTION

APPENDIX A. EXPERIMENTAL SECTION

SEM CHARACTERIZATION

SEM images were taken using a Model Phenom XL (Nanoscience Instruments, Phoenix, Arizona, USA). SEM allows a researcher to view the surface of a sample on the scale of a few micrometers down to nanometer resolution. It is ideal for uncovering micro and nano features on the surface of a sample. Additionally, the conductivity of the species on the surface can give some additional indication of the composition of various features. The conductance data is paired well with EDS, which allows for elemental identification of surface materials based on each element's unique emission spectrum.

Although rare, there were several instances of anisotropic features within the sheet region of the deposition. The features seemed to have defined shapes that corresponded with the angle of incidence and the distance from the strike plate (see Figure A-1). However, without additional studies, it is difficult to ascertain the exact reason behind these features

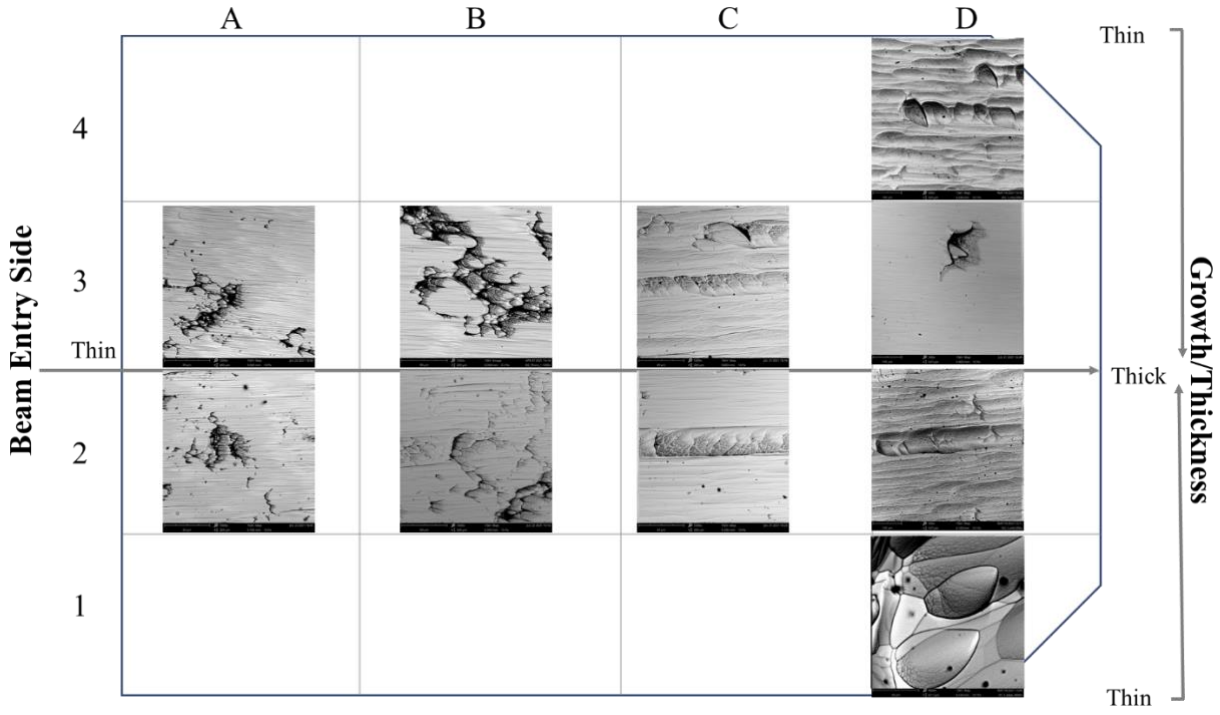

Figure A-1. Different shaped features within the sheet region of the deposition.

Additional images of all features listed in the document are available upon request, including varying magnifications and additional examples of the various features.

EDS, which is attached to the SEM, was used to understand the elemental composition of the surfaces captured in the SEM images. Figure A-2 shows an example of EDS spectrum from Figure 4.

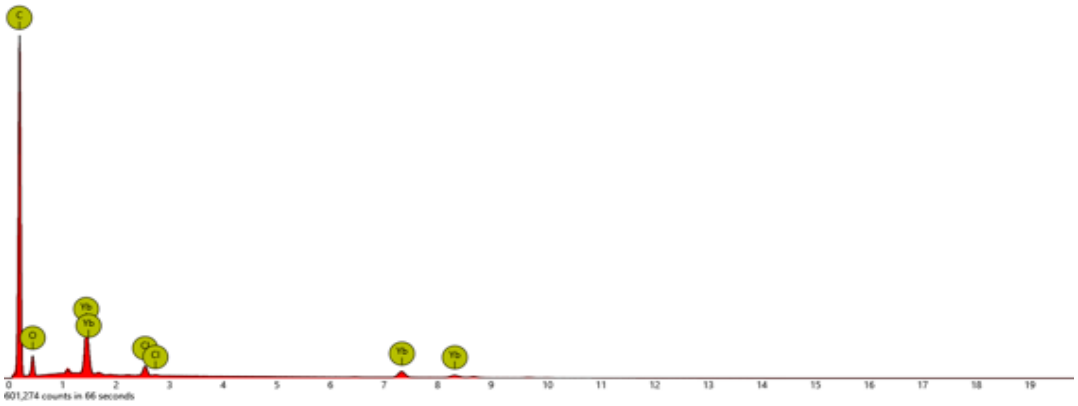

Figure A-2. EDS spectrum of glob region in Figure 4.

XPS CHARACTERIZATION

XPS characterization was conducted using a Model K-Alpha (Thermo Scientific, Waltham, Massachusetts, USA) 1486.6 eV K_α Al x-ray. Samples were mounted on double-sided tape and loaded into the XPS analysis chamber through a vacuum load-lock. Wide energy survey scans were taken, as well as narrow energy range core-level spectra for Yb, C, and O.

This technique uses x-rays to irradiate a solid surface. The photon energy can be imparted to a core-level electron of the inner shell and cause it to be emitted, the so-called "photoelectron". The kinetic energy of the outgoing photoelectron is measured, and by using the photon energy (1486.6 eV K_α Al x-ray) the kinetic energy is converted into binding energy. An XPS spectrum is created by plotting the distribution of photoelectron peaks vs. binding energy in eV. The emitted photoelectrons observed are those originated from the surface layer since the mean escape depth is only a few atomic layers thick. The emitted photoelectrons are characteristic of the energy level of the electron shell of the atom from which it was emitted. In addition to photoelectrons, low-energy Auger electrons can also be emitted; however, by a different mechanism and provides useful information about the surface. An Auger electron is a 3-electron process wherein (1) a core electron is emitted, (2) an outer shell electron fills the hole that was created, and then (3) that electron transfers its energy to another outer shell electron that is emitted (i.e., the Auger electron). The range from 0 to 30 eV on the binding energy scale is the range referred to as the valence band region. Valence band spectra are used routinely as a fingerprint of the studied material. The uniqueness of this technique is that it allows for a detailed study of the surface atomic composition, oxidation state, reactivity, and structure of a substrate.

The d-parameter is obtained from the first derivative of the C-KVV Auger peak by measuring the difference between the Auger peak maximum and minimum. This parameter has shown to be highly sensitive to changes in carbon hybridization. For example, pure diamond, which is composed of amorphous C(sp^3), typically has a d-parameter of 13 eV. Pure graphite (i.e., fully crystalline all sp^2 carbon) has a d-parameter of 24 eV.

RAMAN CHARACTERIZATION

Raman characterization was performed using Renishaw Invia Raman with a diode-pumped solid-state laser at 532 nm (Renishaw, West Dundee, Illinois, USA) at 10% maximum power to avoid damaging the sample's surface. This nondestructive technique provides detailed information about the chemical

structure and even the microstructure of a material (e.g., graphite).[33] This information is carried in scattered light that has interacted with chemical bonds, known as Raman scattering. The peaks in a Raman spectrum are related to specific molecular bond vibrations within the material. Cumulative Lorentzian fit was used to obtain peak position, intensity, and FWHM. The following Tuinstra and Koenig equation was used to calculate the in-plane crystallite size, L_a.

$$L_a = C(\lambda)(I_D/I_G)^{-1} \ ,$$

where $C(\lambda) = 4.956$ at 532 nm .

$$C(\lambda_L) \approx C_0 + \lambda_L C_1, \text{ where } C_0 = -126 \text{ Å and } C_1 = 0.033$$